Nuclear Science and Techniques (2026) 37:121
https://doi.org/10.1007/s41365-026-01930-5

Simulation studies of the directivity in detection of solar neutrinos using deep seawater

Yan Zhou[1] · Da-Wei Si[1] · Sheng Xiao[1] · Jun-Huai Xu[1] · Yu-Hao Qin[1] · Xin Chen[1] · Zhi-Gang Xiao[1]

Received: 13 January 2025 / Revised: 5 July 2025 / Accepted: 8 July 2025 / Published online: 11 April 2026

Abstract
The Čerenkov detector has a distinct advantage in constructing the reaction vertex and incident direction of energetic particles, thereby enabling the identification of emission sources. A novel approach is proposed to measure neutrino sources by employing a modular photomultiplier tube (PMT) array, utilizing clean and transparent deep seawater as the sensitive medium. The feasibility of detecting solar neutrinos was demonstrated through extensive simulations using the Geant4 package. These simulations incorporate the production and transport of Čerenkov photons generated by electron scattering, with the Hough transform method applied to enhance the accuracy of the vertex and direction reconstruction, particularly in the presence of noisy or incomplete data. The dominant background from γ-radiation due to ^{40}K in seawater can be suppressed by a factor of 10^7 by introducing a threshold on the number of triggered PMTs. The total reconstruction efficiency increases with the incident energy, achieving 25% for 6 MeV neutrinos and 52% for 10 MeV neutrinos. For source localization, a sufficient number of neutrino events must be detected, depending on the background intensity above the threshold. The Hough transform was also applied to manage high noise levels during this process. The simulation results confirm the feasibility of detecting solar neutrinos using deep seawater, paving the way for future underwater neutrino detection systems.

Keywords Neutrino · Čerenkov · Geant4 · Energy resolution · Direction reconstruction · Hough transform

1 Introduction

Neutrinos with energies of a few MeV or higher are the major products of nuclear reactions, originating from the Sun (ν_e) or terrestrial nuclear reactors ($\bar{\nu}_e$). Detecting these neutrinos from the Sun provides a critical test of the Standard Solar Model (SSM) and led to the discovery of neutrino oscillations [1–3]. Conversely, detecting anti-electron neutrinos helps monitor nuclear reactor operations [4–12] and constrain the oscillation angle θ_{13} between the first and third generation neutrinos [13, 14]. Despite their importance, detecting neutrinos is extremely challenging because of their weak interactions and small cross-sections. Nevertheless, numerous neutrino detectors have been developed since the first direct detection of neutrino events [15–20]. While the inverse beta decay (IBD) method is widely used for detecting $\bar{\nu}_e$, ν_e detection can be achieved through ν_e–e^- elastic scattering. A key advantage of this scattering process is that the direction of the recoil electron closely aligns with the incident neutrino direction, depending on the neutrino energy [21, 22].

The water Čerenkov detector is a widely utilized neutrino detection technique. For example, the Super–Kamiokande detector (Super-K) employs approximately 40 kT of pure water to successfully detect solar neutrinos, supernova neutrinos, and cosmic ray neutrinos [23]. In this setup, when a recoil electron gains sufficient kinetic energy to move faster than the speed of light in water, it emits Čerenkov radiation at a specific angle, which is then detected by photomultiplier tubes (PMTs) with high timing resolution. By reconstructing the vertex and trajectory of the recoil electron, the direction of the incident neutrino can be inferred [24].

This work was supported by the Ministry of Science and Technology (Nos. 2023YFC3107401) and Tsinghua University Initiative Scientific Research Program.

✉ Yan Zhou
zhou-y21@mails.tsinghua.edu.cn

✉ Zhi-Gang Xiao
xiaozg@tsinghua.edu.cn

[1] Department of Physics, Tsinghua University, Beijing 100084, China

However, increasing the detector volume to improve the event rates becomes technically challenging in land-based laboratories. To achieve the mega-scale detection volumes required for detecting $\nu_e{-}e^-$ scattering events, it has been proposed to use clean seawater or ice at the South Pole as the target material [25, 26]. This approach has been successfully implemented for the detection of extremely high-energy neutrinos in various experiments [27–32]. Extending this method to lower energy domains remains challenging because of the intense background radiation from natural sources such as ^{40}K and ^{208}Tl [33], as well as other radioactive isotopes produced by cosmic ray interactions. Extensive simulation studies are essential to understand the feasibility of detecting low-energy neutrinos using seawater.

This study investigated the feasibility of detecting solar neutrinos using seawater as the target material through Monte Carlo simulations. This study focused on reconstructing the incident direction of neutrinos using faint Čerenkov light signals and suppressing intense radiation backgrounds. The remainder of this paper is organized as follows: Sect. 2 introduces the software, detection array construction, and optical process modeling. Section 3 presents the event reconstruction method, which considers the influence and suppression of background radiation in seawater. Section 4 describes the positioning of the neutrino source, and specifically discusses the physical effect of using clean seawater. Section 5 provides a summary.

2 Simulation software

The simulations were carried out using the WCSim framework [34], a comprehensive simulation environment also used by the Super-K collaboration based on the Geant4 toolkit. This framework provides a complete set of functionalities, including detector geometry modeling, particle transportation from neutrino interactions in water, Čerenkov light generation and propagation, and PMT response modeling. This section outlines the proposed simulation workflow.

2.1 Detector constructions

In the current application, water is defined as an absorbing material. The PMTs are distributed in a specific configuration to detect the Čerenkov light emitted by the high-speed electrons produced in neutrino-induced reactions. For simplicity in the startup simulation, a spherical distribution of PMTs was adopted in water. This configuration was chosen to ensure isotropic detection capabilities, which are essential for locating an unknown source. The radius of the sphere, measured at the front surface of the PMTs, was set to $R = 5$ m. This value is reasonable and feasible for constructing a demonstrator while also providing a sufficiently large fiducial volume. Given the lack of an analytical solution for a series of points uniformly distributed on a sphere, the setup employs an approximate solution based on the Fibonacci grid [35]. The spherical coordinate angles θ_i and ϕ_i of the i^{th} PMT are given by Eq. (1).

$$\begin{cases} \cos\theta_i = \frac{2i+1}{N} - 1 \\ \phi_i = (\sqrt{5} - 1)i\pi \end{cases} (i \in [1, N]) \tag{1}$$

The symmetrical axis is aligned with the center of the sphere. The diameter of the sensitive area of each PMT is $\phi_{\text{pmt}} = 8$ in. Assuming a 30% coverage of the entire sphere surface, which represents a moderate and achievable value, 2906 PMTs were constructed. The physical construction of each PMT was simplified as a glass bulb containing a vacuum. The remaining area of the sphere was covered with black sheets to minimize internal reflections, and the surface reflectivity was manually adjusted to 95% from the inner to outer space. To mitigate the residual radiation from the PMT materials, the fiducial volume was defined by a sphere with a radius of $R_{\text{fd}} = 4.5$ m. Figure 1 presents the schematic view of the PMT sphere. The distance between neighboring PMTs was maintained at 30–40 cm.

2.2 Simulation of the optical process by incident electron

The simulated event began with the generation of a charged particle in a neutrino-induced reaction. This process is enforced because of the low cross-section of weak interactions, which makes it challenging to achieve sufficient statistics using conventional sampling techniques. Charged particles lose energy in water and emit Čerenkov light if their velocity exceeds the threshold. The simulation tracked all secondary particles until they were stopped or absorbed. Čerenkov photons in water undergo scattering and absorption according to the optical parameters of the medium. If a photon reaches the PMT surface, it can generate a certain number of photoelectrons (PEs) and produce a signal based

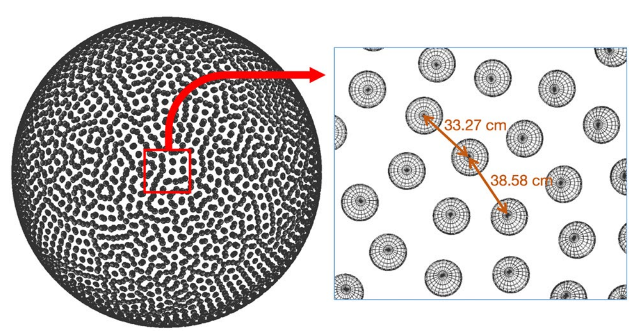

Fig. 1 (Color online) The schematic view of the PMTs distributing on a sphere filled by water

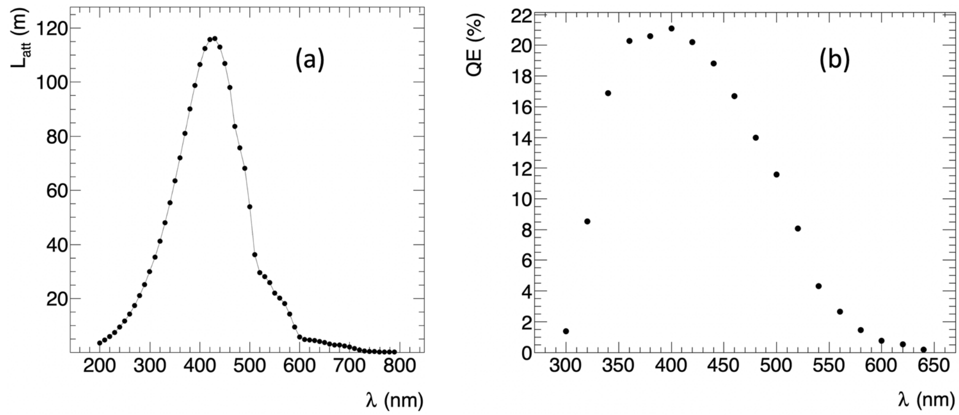

Fig. 2 Parameters used in the simulation package. The data were obtained from [34]. **a** Attenuation length as a function of the photon wavelength. **b** PMT quantum efficiency as a function of photon wavelength

on the PMT response parameters. Alternatively, photons may be absorbed if they strike a black surface outside the PMT acceptance range.

In this study, the PMT response settings were identical to those of the Super-K experiment [36]. If more than 10 PMTs were triggered within 50 ns (representing the time it takes for light to traverse the entire detector), a trigger signal was generated, and the data were stored for further analysis. Therefore, the transport and absorption of Čerenkov photons are critical processes in the detection mechanism. The detection process is governed by several optical parameters for the medium and surfaces, including the absorption length, refractive index, and scattering length. These parameters are dependent on the photon wavelength. For simplicity, the parameter set of water was adopted from Super-K [36], which is suitable for pure water but may not be ideal for seawater. The effect of seawater is discussed in Sect. 4.

The attenuation length is shown in Fig. 2a, where the value in the blue wavelength band is about 100 m, the refractive index is 1.334. Additionally, the refractive index for glass was set to 1.6, and the absorption length for a black sheet was set to 10^{-11} m. The surfaces are defined as the interfaces between these media. The reflectivity between the water and black sheet was set to 0.05. The quantum efficiency of the PMTs is a function of the photon wavelength, as shown in Fig. 2b. The maximum efficiency was 21.1% at $\lambda = 400$ nm.

Figure 3 illustrates an event display of the optical process resulting from a 6 MeV electron neutrino-induced reaction. The incident direction was randomly distributed over a 4π solid angle, with the vertex fixed at the center. The red lines represent the tracks of Čerenkov photons, while the dashed arrow indicates the direction of the recoil electron, which is expected to be reconstructed from the PMTs triggered by photons. Photons absorbed by the water or sphere surface were lost and excluded from the analysis.

The correlation between the number of photons triggering the PMTs and the total number of photons produced in each neutrino-induced reaction is illustrated in Fig. 4. The simulation incorporates dark noise at 4.2 kHz, which is typical in PMTs, and may result in 1–2 additional signals per event. The overall efficiency of the PMT triggering was approximately 20%. Considering the geometric coverage of about 30%, it is inferred that roughly 40% of the photons are lost during transport to the PMTs owing to scattering or absorption.

The limited distribution of Čerenkov photons is crucial for event reconstruction at the event-by-event scale. The distribution of Čerenkov photons in a polar coordinate system θ vs. ϕ is shown in Fig. 5. Here, θ is the angle between the direction of the recoil electron and the vector from the reaction vertex to the triggered PMT, and ϕ is the azimuthal angle of the Čerenkov photon. Figure 5a displays the cumulative θ vs. ϕ plot for 10^5 events, with the electron's incident

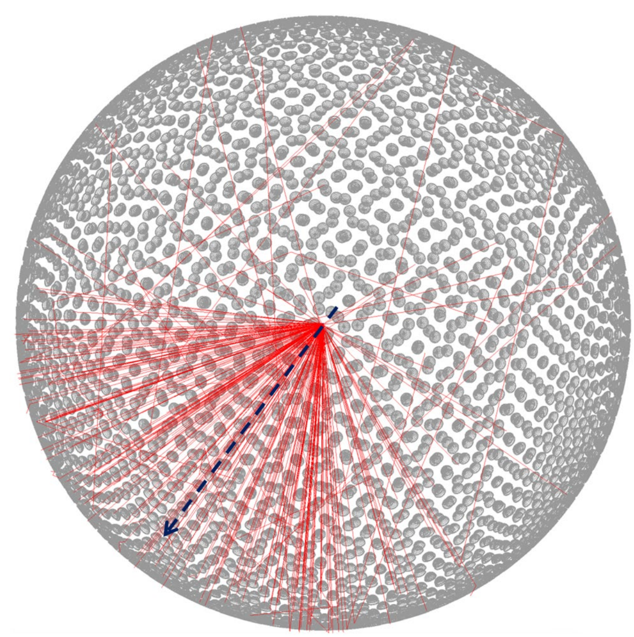

Fig. 3 (Color online) One event display induced by a 6 MeV electron neutrino. The red lines are the tracks of the Čerenkov photons, and the thick dashed black arrow denotes the recoil electron in ν_e–e^- scattering

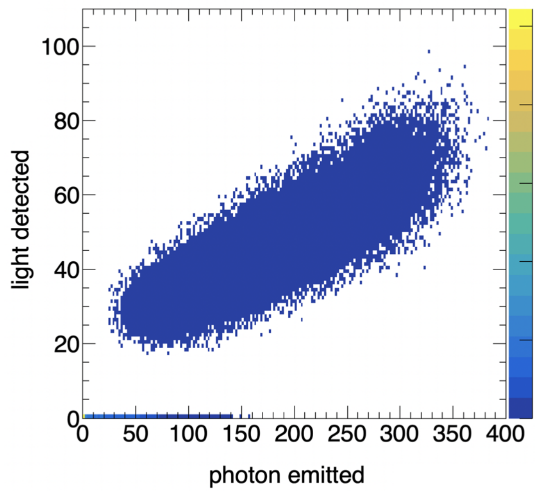

Fig. 4 (Color online) The correlation of the number of the emitted Čerenkov photons and the detected ones

direction pointing to the pole ($\theta = 0°$) by definition. The Čerenkov circle is clearly visible, with its center at $\theta = 0°$. However, for individual events, as shown in Fig. 5b and c, the triggered PMTs are distributed in a scattered manner, making the circular pattern invisible to the eye. This necessitates a sophisticated algorithm to reconstruct the direction of incident electrons.

2.3 More discussions on seawater environment

The tropical deep-sea neutrino telescope (TRIDENT) collaboration [37] measured an attenuation length of 20 m in the blue wavelength band at a depth of 3.5 km. This is considerably shorter than the 100 m reference value used in Fig. 2a. For a typical photon travel distance of 5 m, the survival probability in seawater compared to that in pure water is $\eta = e^{-\frac{5\ \mathrm{m}}{20\ \mathrm{m}}}/e^{-\frac{5\ \mathrm{m}}{100\ \mathrm{m}}} = 82\%$. Although this corresponds to an 18% reduction in photon yield, the current PMT threshold $M_{\mathrm{pmt}} \geq 20$ (see Sect. 3.4) effectively rejects ^{40}K backgrounds; therefore, the overall conclusions remain unaffected.

Impurity ions in seawater can induce background reactions, such as $\nu_e + {}^{37}\mathrm{Cl} \rightarrow e^- + {}^{37}\mathrm{Ar}$, with a cross-section of $\sigma_{\mathrm{Cl}} = 1.14 \times 10^{-42}\ \mathrm{cm}^2$ [38]. Given a chloride concentration of 0.546 mol/L and an isotopic abundance of ^{37}Cl ($\eta_{37} = 24.23\%$), the additional background-to-signal ratio was estimated to be approximately 0.5% using Eq. (2).

$$\mathrm{ratio} = \frac{\eta_{37}\ \rho_{\mathrm{Cl}}\ \sigma_{\mathrm{Cl}}}{\rho_e\ \sigma_e} = 0.5\% \tag{2}$$

This value is negligible; however, future studies should consider the uncertainties in these parameters.

For biofouling mitigation, PMTs are oriented inward within a light-shielded detector design, which minimizes exposure to light induced by external biofouling. Because biofouling emissions are omnidirectional, unlike the directional Čerenkov radiation generated by neutrino-related signal events, this difference enables effective discrimination. Consequently, biofouling does not impose a significant challenge to current feasibility simulations.

3 Event reconstruction

This section presents a detailed description of the reconstruction procedure for the ν_e–e^- scattering process. The primary objective of this reconstruction is to accurately determine the timing and vertex of the scattering event based on the detected Čerenkov photons in the detector [39–43].

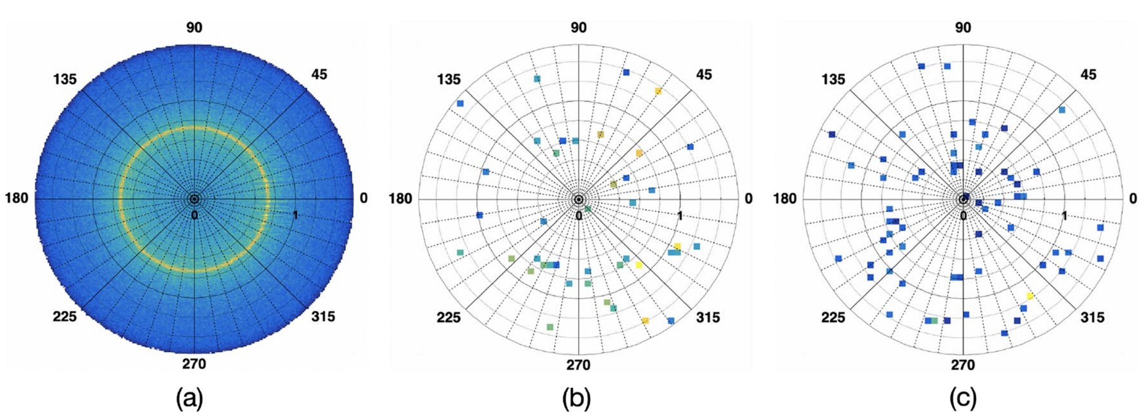

Fig. 5 (Color online) Projection diagram of fired PMTs relative to the recoil electron direction. **a** Integration over 10^5 events. **b** and **c** Fired PMT distributions in two single events

3.1 Vertex reconstruction

This study focused solely on the $\nu_e - e^-$ elastic scattering process. The determination of the vertex position depends on the timing information obtained from the fired PMTs. Consequently, the time resolution is a critical parameter. For neutrinos with a few MeV of kinetic energy, the recoil electron rapidly loses all its kinetic energy, resulting in a negligible track length. Therefore, all Čerenkov photons are assumed to originate from a single point denoted as (x_0, y_0, z_0, t_0). Given the exact position (x_i, y_i, z_i) of each fired PMT, the expected arrival time t_i^{exp} of the Čerenkov photon at the i^{th} PMT can be calculated as:

$$t_i^{\mathrm{exp}} = t_0 + \frac{|\mathbf{r}_i(x_i, y_i, z_i) - \mathbf{r_0}(x_0, y_0, z_0)|}{c/n}, \tag{3}$$

where c is the speed of light in vacuum, and n is the refractive index of water.

If the reconstructed vertex coincides with the true vertex, the difference between the recorded firing time and the expected time (from Eq. (3)) for all fired PMTs should yield a sharp peak centered at zero. However, if the reconstructed vertex deviates from the true position, the calculated time distribution exhibits a broader and distorted distribution with large timing residuals.

To address this, the vertex parameters that maximize the consistency between the measured and expected times should be selected, thereby yielding the final reconstructed vertex. Specifically, the strategy is to minimize the function defined in Eq. (4) [44]

$$f = \sum \exp\left(-\zeta_i^2/\sigma_{\mathrm{t}}^2\right), \tag{4}$$

where $\zeta_i = t_i - t_i^{\mathrm{exp}}$ represents the deviation of the measured time t_i from the expected time t_i^{exp}, and $\sigma_{\mathrm{t}}^2 = 50$ corresponds to the PMT time resolution.

It should be noted that the ansatz in Eq. (4) without the exponential term resembles a conventional χ^2 value. The inclusion of the exponential term is motivated by the fact that some Čerenkov photons may undergo multiple reflections before reaching a PMT, causing the actual firing time to differ significantly from the value predicted by Eq. (3). This exponential term reduces the sensitivity of the fit to such outliers, enabling a more robust reconstruction of the vertex based on an event-by-event logic.

3.2 Direction construction

The Čerenkov lights generally form a cone with a semi-apex angle satisfying $\sin\alpha = (n\beta)^{-1}$, where $\beta = v/c$ and v is the particle velocity. For electrons with energies of several MeV, the distance traveled before slowing down to the threshold is short (approximately 1 cm). As a result, the emitted Čerenkov lights can be approximated to have a fixed emission angle from the reaction vertex, given by $\alpha_{\mathrm{c}} \approx \arcsin(n^{-1})$. However, secondary scattering of electrons in the medium causes broadening of the angular distribution, as shown in Fig. 6. This distribution is used as the probability distribution function (PDF) in the Hough transform.

The Hough transform (HT) method [22, 45–48] was applied to determine the direction of the recoil electron in $\nu_e - e^-$ scattering using data recorded by the PMTs. Figure 7 illustrates an example of the HT method applied to the event shown in Fig. 5b. Once a vertex is reconstructed, each fired PMT defines a direction vector characterized by the polar angle θ_i and azimuth ϕ_i. To simplify the explanation, consider the fixed Čerenkov angle (α_{c}) first. For each PMT, the data point generates a circle on the $\theta - \phi$ plane at the given polar angle α_{c}, with the longitudinal axis aligned from the vertex to the fired PMT, as shown in Fig. 7a by red cross symbols. This circle represents a probability distribution in the parameter space of the electron direction, characterized by θ_0 and ϕ_0. As shown in Fig. 7b, summing the transformed probability distributions weighted by the number of PEs from all fired PMT data points yields the probability distribution of the high-speed electron in the $\theta - \phi$ parameter space. The most probable point in this distribution corresponds to the reconstructed direction of the electron. In real calculations, owing to the scattering of Čerenkov photons, the PDF of the Čerenkov angle from Fig. 6 is used instead of a fixed α_{c}. Following the same procedure, with the circle replaced by the continuous distribution for each transformation, the real probability distribution of the direction in the $\theta - \phi$ parameter space is obtained. The most probable point $\theta_0 - \phi_0$ is situated at the point with the highest probability, as depicted by the red cross marker in Fig. 7c.

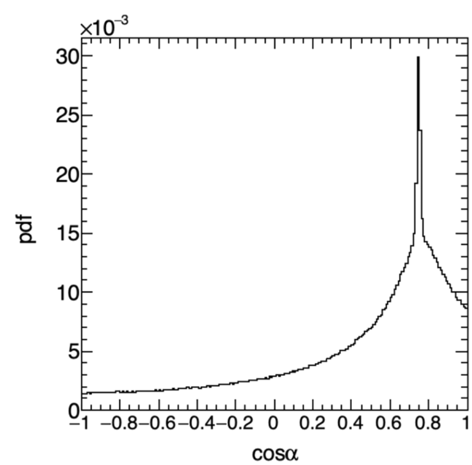

Fig. 6 Angular distribution of Čerenkov lights with respect to the electron flying direction

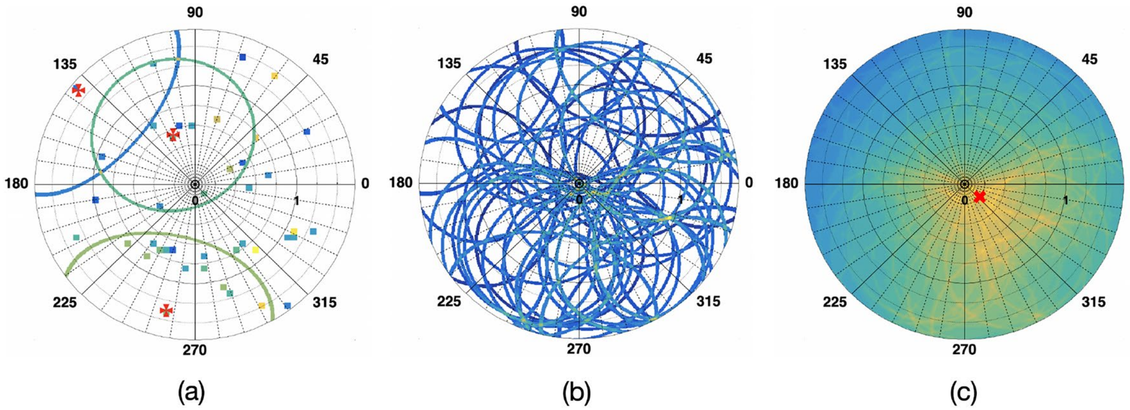

Fig. 7 (Color online) Schematic elucidation of the Hough Transform method. **a** The fired PMTs on $\theta-\phi$ plane, the circles near the red cross markers are the possibility distribution to find the electrons, assuming a constant Čerenkov angle. **b** All the possibility distributions are summed up for all fired PMTs with the number of PE as the weight. **c** The real possibility distribution of finding the electron in $\theta-\phi$ parameter space, using the PDF shown in Fig. 6. The red cross marker represents the recognized direction of the electrons

3.3 Result from neutrino events

In neutrino-induced reaction simulations, the issue of insufficient statistics owing to the small cross-section is addressed by forcing the reaction to occur when a neutrino is injected. The distribution of recoil electrons is sampled using Eq. (5) [49],

$$\frac{\mathrm{d}\sigma}{\mathrm{d}\cos\theta} = \frac{4\sigma_0 E_\nu^2 M^2 \cos\theta}{(M^2 - E_\nu^2\cos^2\theta)^2} \times \left[g_1^2 + g_2^2\left(1 - \frac{T_e}{E_\nu}\right)^2 - g_1 g_2 \frac{m_e T_e}{E_\nu^2}\right], \tag{5}$$

where T_e represents the kinetic energy of the recoil electron.

$$T_e = \frac{2m_e E_\nu^2 \cos^2\theta}{M^2 - E_\nu^2\cos^2\theta} \quad , \quad M = m_e + E_\nu. \tag{6}$$

The constants g_1 and g_2 characterize the coupling strength of the left- and right-handed components in weak interactions and are dependent on the flavor of the neutrino. The corresponding distribution for solar neutrinos ν_e is shown in Fig. 8.

The simulation process proceeds as follows: a random point within the fiducial volume of the detector setup is selected as the reaction vertex. The scattering angle is randomly sampled from Eq. (5) for a given neutrino energy, and the electron momentum was calculated using energy-momentum conservation. The vertex and momentum together define the recoil electron as a neutrino event. Subsequently, Čerenkov light is generated based on the velocity of the recoil electron and transported to the PMTs, where the emitted PEs are recorded. The HT method is then applied to

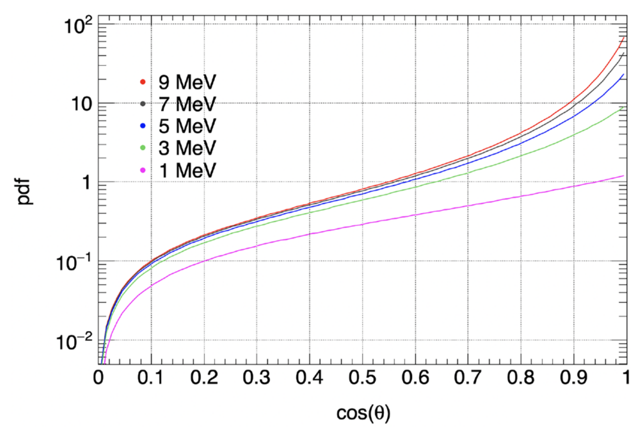

Fig. 8 (Color online) Angular distribution of the recoil electron in ν_e-e^-scattering with respect to the incident direction of the neutrino at different E_ν

reconstruct the incident direction of the recoil electron and the position of the reaction vertex.

The results of the reconstruction are shown in Fig. 9. For each energy point, 10^5 events were simulated. Figure 9a shows the distribution of α, defined as the angle between the reconstructed and genuine directions of the recoil electron. As the incident neutrino energy increases, the energy of the recoil electron also increases, and the distribution exhibits a more pronounced peak at $\cos\alpha = 1$, indicating a higher reconstruction success. The efficiency ηincreases from 0.66% at $E_\nu = 2$ MeV to 66% at $E_\nu = 10$ MeV. Figure 9b displays the mean value $\langle\cos(\alpha)\rangle$ as a function of the incident neutrino energy. At the high-energy end near 10 MeV, $\langle\cos(\alpha)\rangle = 0.76$, suggesting a good determination of the electron direction. Figure 9c presents the distance ΔR between the genuine and reconstructed reaction vertices. The

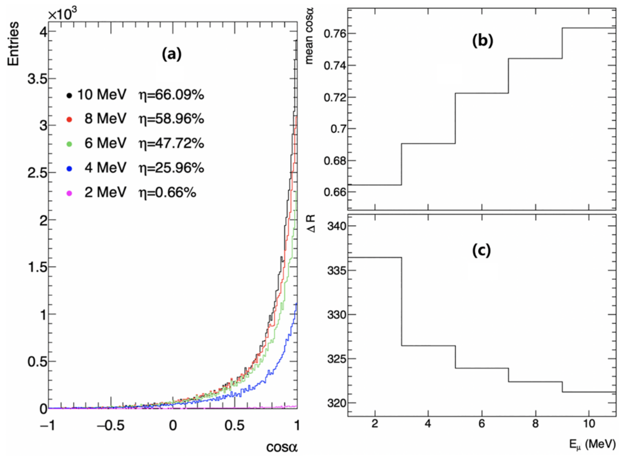

Fig. 9 (Color online) **a** Distributions for angle reconstruction with their efficiency. **b** and **c** show the mean value of $\langle\cos(\alpha)\rangle$ and the error of the constructed vertex as a function of the neutrino energy

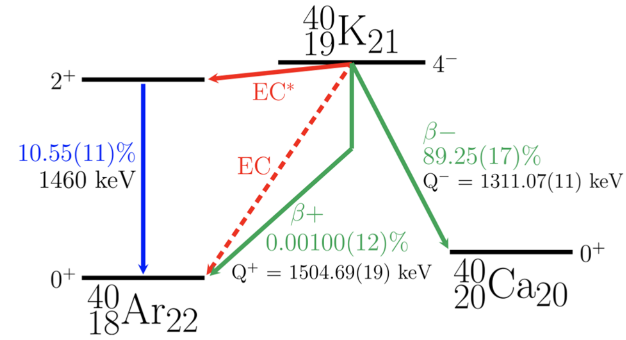

Fig. 10 (Color online) The decay scheme of ^{40}K [54]

deviation of the reconstructed vertex decreased slightly as a function of the incident neutrino energy E_ν.

3.4 Influence of the background events

Careful treatment is required to suppress events caused by intense background sources, including seawater radioactivity, cosmic ray muons, and faint light emitted by bioluminescent plankton near the detector volume [50]. In principle, the muon background can be efficiently rejected using a veto detector mounted above the main detector or by applying an energy cutoff. This is because the Čerenkov photons produced by energetic muons penetrating the thick seawater are abundant. Additionally, light from bioluminescent plankton induces signals on PMTs with distinct rising times and amplitudes, allowing for identification and rejection. However, seawater radioactivity is primarily focused on because the intensity of γ-radiation from radioactive isotopes is high, and their γ energy is comparable to the recoil electron energy in ν_e–e^- scattering, making it the dominant background noise.

The primary radioactive isotope in seawater is ^{40}K [51–53]. The mass fraction of potassium in seawater is $\rho_K = 380$ mg/L, and the isotopic abundance of ^{40}K is $\eta_{40} = 0.0117\%$. The decay lifetime of ^{40}K is $\tau = 5.692 \times 10^{16}$ s. Using Eq. (7), the event rate for ^{40}K is calculated:

$$n = \frac{\eta_{40} \cdot \rho_K \cdot N_A}{M_K \cdot \tau} = 12.03\,\mathrm{L}^{-1}\mathrm{s}^{-1} \tag{7}$$

where N_A is Avogadro's constant, and M_K is the molar mass of potassium. The calculated event rate was significant, necessitating a detailed simulation of the background. ^{40}K has multiple decay channels [54], as shown in Fig. 10.

Specifically, 89.25% of its decays are β^- decays to the ^{40}Ca ground state, and 10.55% are electron-capture transitions to the 1460 keV level of ^{40}Ar. To model the ^{40}K process, a combination of 10.55% of 1.46 MeV γ-ray events and 89.25% of decayed e^- events, with random positions and directions, was simulated. The e^- energy is derived from Eq. (8), with a maximum energy $E_{max} = 1.311$ MeV.

$$\frac{dN}{dE} \propto (E_{max} - E)^2 \sqrt{E^2 + 2m_e E} \tag{8}$$

Because γ-rays can travel a distance before being absorbed, decay events are generated in an extended volume with a radius $R = 6$ m, exceeding the fiducial volume.

Figure 11a–c illustrate the effects of the ^{40}K background. Figure 11a shows the distribution of $\cos\alpha$, where α is the angle between the reconstructed electron and the initial radiation from the source. A forward-peaking feature is evident. Figure 11b displays the displacement between the real and reconstructed vertices. Figure 11c presents the distribution of the number of fired PMTs M_{pmt} caused by ^{40}K events.

Another major radioactive source in seawater arises from the decay chain of ^{232}Th and ^{238}U. The most energetic γ-ray in this chain is the 2.6 MeV γ-ray from ^{208}Tl. To be conservative, the study simulates the background using 2.6 MeV γ-radiation. The results are shown in Fig. 11d–f. The features of the 2.6 MeV γ-rays are similar to those of the ^{40}K decay, except that the multiplicity of fired PMTs M_{pmt} is slightly higher for the 2.6 MeV γ-rays, as seen in the peak positions.

Unfortunately, whether the detected particle is an e^- or a γ-ray, it is always observed as an e^-, identical to the ν_e–e^- scattering event. The only distinction between the signal and background lies in the e^- energy. To differentiate the neutrino signal from the background, a cut was imposed on M_{pmt} to suppress events caused by the intense radioactive sources in the seawater. Figure 12a shows the multiplicity

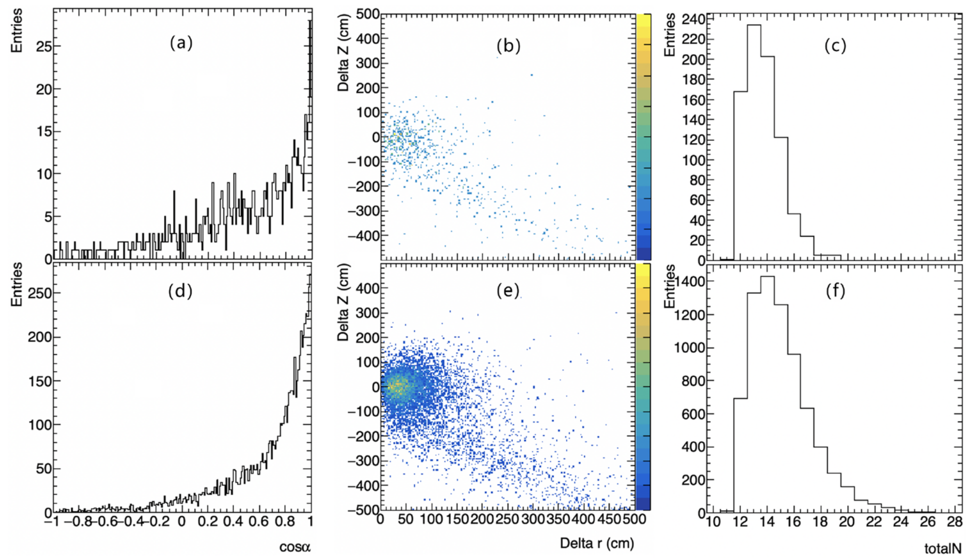

Fig. 11 (Color online) Left: The distribution of the angle between real and constructed direction of ^{40}K decay (**a**) and γ-rays at $E_\gamma = 2.6$ MeV (**d**). Middle: distribution of the deviation between the real and constructed vertices in the coordinate space for ^{40}K decay (**b**) and γ-rays at $E_\gamma = 2.6$ MeV (**e**). Right: the distribution of the multiplicity of fired PMTs for ^{40}K decay (**c**) and γ-rays at $E_\gamma = 2.6$ MeV (**f**)

distribution as a function of the incident neutrino kinetic energy E_ν. The goal is to reject the ^{40}K background owing to its extremely high event rate. Based on Fig. 11c, a threshold condition of $M_{\text{pmt}} \geq 20$ is set, as indicated by the dashed line in Fig. 12a. As the neutrino energy increases, more events are accepted. For $E_\nu = 6$ MeV and 10 MeV, the ratios of events with M_{pmt} above the threshold are 55% and 80%, respectively, as shown in Fig. 12b. After filtering, the construction efficiencies were 25.6% and 52.2%, respectively, which remained acceptable for detection. The events induced by the ^{40}K background are suppressed by a factor greater than 10^7.

4 Neutrino source reconstruction

With the background suppression scheme, a simple application can be considered to identify an existing neutrino emission source, using the Sun as an example. Genuine neutrino-induced events are overwhelmed by intense background radiations. While the suppression factor for ^{40}K radiation is 10^7, the dominant background is not necessarily ^{40}K. Instead, the remaining background could include 2.6 MeV γ-rays from ^{208}Tl, ^{40}K decays that pass the cuts, neutrino events from other potential sources, and other unaccounted backgrounds.

The event rates for these backgrounds remain unknown until they are tested in a realistic scenario. Fortunately, the background events were isotropic. Therefore, if a background event passes the cuts, it can be manually added to the final data spectrum with an arbitrary incident direction. Simultaneously, neutrinos from the source position trigger ν_e–e^- scattering events, producing recoil electrons that emit Čerenkov photons along specific directions, as shown in Fig. 8. To infer the location of the ν_e source, a sufficient number of ν_e–e^- scattering events must be accumulated, and the Hough transform must be performed again.

Once the electron direction is reconstructed from the fired PMTs, the Hough transform can be applied using the probability distribution defined in Eq. (5). Figure 13 illustrates the transformation process in θ–ϕ space. Each data point represents the reconstructed direction of a single event. A total of 1000 events were used for the search. In Fig. 13a and b, all events are neutrino signals, while in Fig. 13c and d, the background-to-signal ratio is set to 5:1, with background events (83%) randomly sampled from all directions. The input source direction was set at an angle of 45° relative to the axis to test the homogeneity of the detector, with initial directions $\theta = 135°$ and $\phi = 90°$. In Fig. 13a, the dense population of events near the set value is distinguishable even by eye. Figure 13b shows the corresponding Hough transform result, with the most probable reconstructed position at $\theta = 137.3°$ and $\phi = 89.1°$ (red star). The principle of HT here is the same as that used to construct the event direction in Sect. 3.2, with the probability distribution for the HT procedure changed to Eq. (5) instead. In Fig. 13c, it is much harder to identify the source from the data distribution plot alone. However, the Hough transform results in Fig. 13d reconstructs the direction as $\theta = 140.8°$ and $\phi = 80.1°$, deviating by only 8.8° from the initial direction.

4.1 Sun locating attemption

The search capability of the detector can be evaluated using the Sun as a neutrino source. The solar neutrino flux and corresponding event rate in the proposed detector design were estimated. In this analysis, the Sun's apparent motion

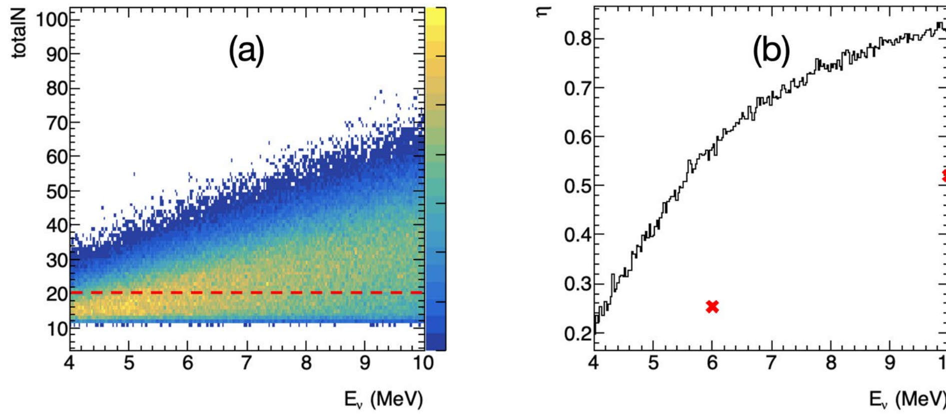

Fig. 12 (Color online) **a** Distribution of multiplicity of fired PMT number as a function of neutrino energy E_ν. **b** Ratio of events above the M_{pmt} as a function of E_ν. The final reconstruction efficiency after HT transformation for 6 MeV and 10 MeV neutrino is indicated by the red cross symbol

was neglected by adopting a space-fixed coordinate system anchored to distant stars rather than an Earth-fixed frame. The solar neutrino flux for $E_\nu \geq 6$ is approximately $\Phi = 2.5 \times 10^6\,\text{cm}^{-2}\text{s}^{-1}$ [55]. The energy-dependent cross-section for ν_e–e^- elastic scattering is given by Eq. (9) [49].

$$\sigma = 93(E_\nu/\text{MeV}) \times 10^{-46}\text{cm}^2 \tag{9}$$

The event rate is calculated as follows:

$$n = \rho\sigma\Phi = 0.005\,\text{m}^{-3}\text{day}^{-1} = 2\,\text{module}^{-1}\text{day}^{-1} \tag{10}$$

where $\rho = 0.56 \times 10^6 N_\text{A}$ is the electron density in water.

Considering a construction efficiency of 33% (as described in Sect. 3.4), we expect approximately 20 detected neutrino events per module per month. With 15 detector modules, 300 solar neutrino events per month can be obtained from the same direction. For the background, because most ^{40}K events are excluded by the cuts, a background-to-signal ratio of 50 is reasonable, corresponding to 15,000 background events above the threshold. These background events were randomly sampled in all directions. When these signals and backgrounds were input into the

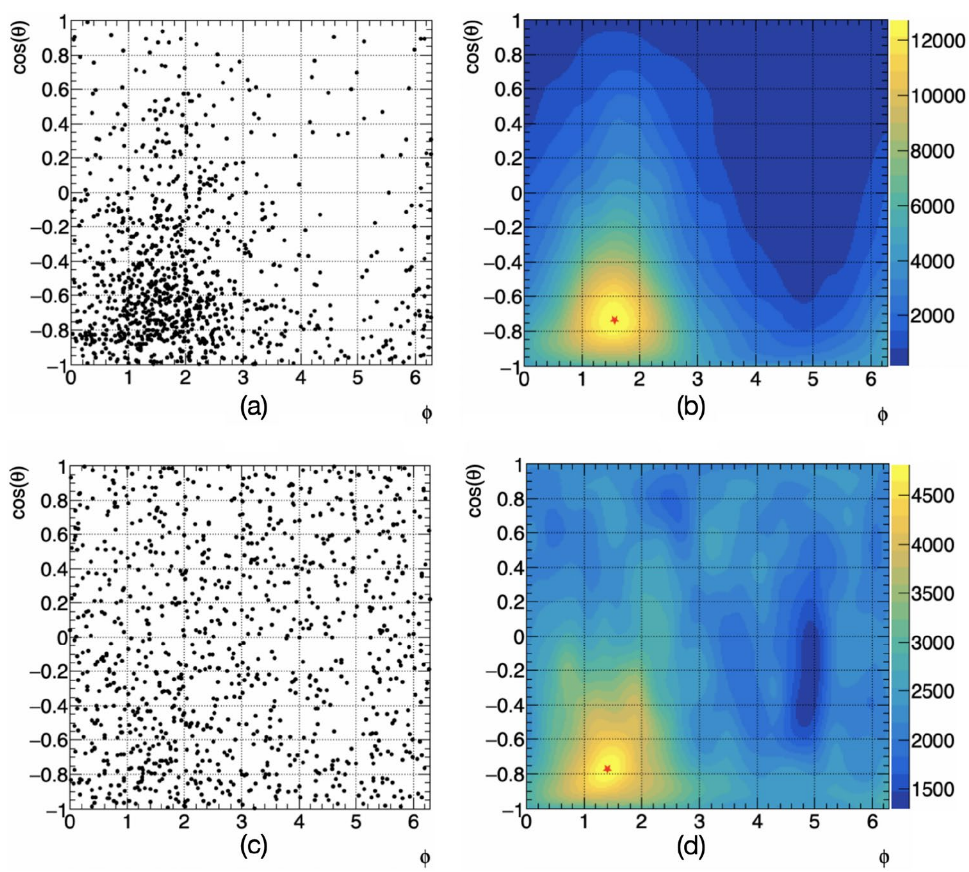

Fig. 13 (Color online) Plot of source searching Hough transform procedure. **a** Data points of 1000 ν_e- e^- events. **b** The corresponding Hough transformed probability distribution in θ and ϕ space. **c** Data points of 1000 events with background-to-signal ratio being 5:1, where the background (83%) are from all directions randomly. **d** The corresponding Hough transformed probability distribution in θ and ϕ space

Hough transform, the source direction could be inferred, as shown in Fig. 13.

To obtain comprehensive results, a statistical ensemble containing 10,000 simulations was performed. The angle Θ_s between the real source direction and the reconstructed direction is illustrated in Fig. 14. The search accuracy must meet the requirements of real-world applications. Now, defining successful reconstruction by $\cos\Theta_s \geq 0.8$ (dashed line), the success rate is approximately 90% for a 30-day search with 300 solar neutrino events and a background-to-signal ratio of 50.

4.2 Searching ability discussion

Given that the detector is capable of searching for multiple neutrino sources, it is critical to optimize the experimental setup, specifically the number of modules, total volume of the sensitive medium, and search duration, as these factors collectively determine the number of collected neutrino signals, even under high background-to-signal ratios. Qualitatively, an increase in neutrino signals improves the search success rate, even at higher background-to-signal ratios.

To achieve the same success condition (i.e., 90% success rate), the minimum number of accumulated events as a function of the background-to-signal ratio was investigated, as shown in Fig. 15. The minimum number of neutrino events $N_\nu^{\mathrm{min}}(90\%)$ required to ensure a 90% success rate is approximately linear with respect to the background-to-signal ratio. For example, if the background-to-signal ratio reaches 270, 1000 neutrino events must be accumulated.

This linear relationship provides confidence that, regardless of how large the background-to-signal ratio becomes, the same search capability can be achieved by scaling the number of detector modules. This is reasonable because the condition for identifying the true source is that the signal

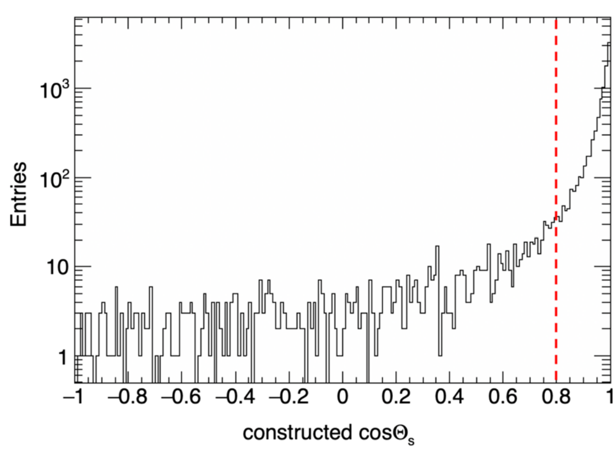

Fig. 14 Distribution of cosine of the angle ($\cos\Theta_s$) between real and constructed neutrino source direction with 10,000 simulated searches

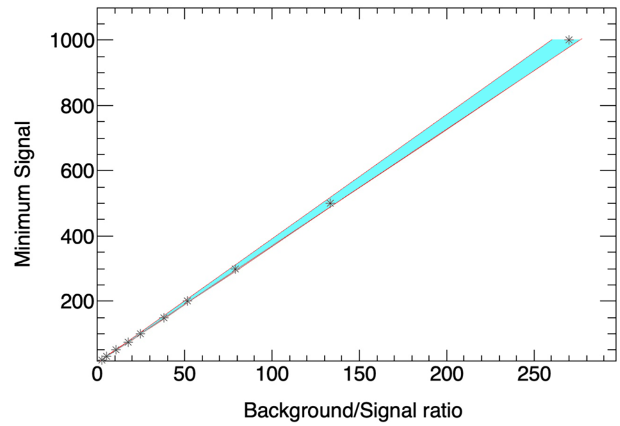

Fig. 15 (Color online) The minimum accumulation of events $N_\nu^{\mathrm{min}}(90\%)$ required to ensure 90% success rate as a function of background-to-signal ratio. The band represents a 99% confidence interval

peak on the Hough transform probability plane exceeds the background fluctuations. Assuming that the signal peak height scales proportionally with the total number of signal events (N_s) and that the background fluctuations scale as $\sqrt{N_b}$, one obtains $N_s \propto \sqrt{N_b}$. With appropriate rescaling, this relationship can be expressed as Eq. (10):

$$N_s = k\left(\frac{N_b}{N_s}\right), \tag{11}$$

where k is a factor that is positively correlated with the success condition. This implies that by increasing the number of detector modules, the increased signal can overcome higher background fluctuations, thereby maintaining a 90% success rate.

5 Conclusion

The feasibility of locating neutrino sources using a deep seawater Čerenkov detector through Geant4 simulations was demonstrated. A spherical water volume instrumented with PMTs was employed as a sensitive detector submerged in seawater. The production and transport of Čerenkov photons generated by the ν_e–e^- reaction were simulated. The vertex and direction of the high-speed electrons producing the Čerenkov photons were reconstructed using the Hough transform. The γ-radiation background in seawater was carefully accounted for, and it was found that setting a threshold on the number of fired PMTs can effectively suppress the background. The reconstruction efficiency of the neutrino increases with neutrino energy and averages approximately 33% for neutrinos in the 6–10 MeV range. To locate an existing neutrino source, a finite number of neutrino events are required, depending on the background intensity above the PMT threshold. With 300 accumulated neutrino events, the source direction can be inferred with angular accuracy $\cos\Theta_s > 0.8$ under a background-to-signal ratio of 50.

The deep-sea environment offers an effective scenario in which the detector volume is treated as unlimited, thereby providing a scalable framework for the detector design. Although an idealized detector configuration, with a virtually unlimited volume and sufficient detector modules, ensures that the direction of an unknown neutrino source can be inferred irrespective of background levels, practical constraints (such as the high cost required to deploy additional modules and achieve a sufficient counting rate) may significantly limit real-world implementations. Furthermore, the accuracy of source reconstruction is inherently linked to the energy of the target neutrino, with lower energy events posing greater challenges for accurate detection and localization. Future research should focus on optimizing key design parameters, such as the detector volume, PMT placement, and coverage rate, to better match the expected energy spectra and event rates of specific neutrino sources. Such optimization would enhance the detection sensitivity and operational feasibility. In conditions where the background-to-signal ratio is excessively high, additional attention is required to accurately identify neutrino events from known sources (e.g., inverse beta decay signals from reactor neutrinos). Future studies should explore alternative background suppression techniques specifically tailored to mitigate distinct background components, thereby improving overall signal discrimination and detection sensitivity.

Author Contributions All authors contributed to the study conception and design. Material preparation, data collection, and analysis were performed by Yan Zhou. The first draft of the manuscript was written by Yan Zhou and all authors commented on previous versions of the manuscript. All authors read and approved the final manuscript.

Data Availability The data that support the findings of this study are openly available in Science Data Bank at https://cstr.cn/31253.11.sciencedb.j00186.00925 and https://www.doi.org/10.57760/sciencedb.j00186.00925.

Declarations

Conflict of interest The authors declare that they have no conflict of interest.

References

1. Y. Fukuda, T. Hayakawa, E. Ichihara et al., Measurements of the solar neutrino flux from Super-Kamiokande's first 300 days. Phys. Rev. Lett. **81**, 1158 (1998). https://doi.org/10.1103/PhysRevLett.81.1158
2. Q.R. Ahmad, R.C. Allen, T.C. Andersen et al., Direct evidence for neutrino flavor transformation from neutral-current interactions in the sudbury neutrino observatory. Phys. Rev. Lett. **89**, 011301 (2002). https://doi.org/10.1103/PhysRevLett.89.011301
3. W. Chen, L. Ma, J.H. Chen et al., Gamma-, neutron-, and muon-induced environmental background simulations for ^{100}Mo-based bolometric double-beta decay experiment at Jinping Underground Laboratory. Nucl. Sci. Tech. **34**, 135 (2023). https://doi.org/10.1007/s41365-023-01299-9
4. H. Furuta, Y. Fukuda, T. Hara et al., A study of reactor neutrino monitoring at the experimental fast reactor JOYO. Nucl. Instrum. Methods A **662**, 90 (2012). https://doi.org/10.1016/j.nima.2011.09.045
5. J. Ashenfelter, D. Sweeney, M. Green et al., The PROSPECT reactor antineutrino experiment. Nucl. Instrum. Methods A **922**, 287 (2019). https://doi.org/10.1016/j.nima.2018.12.079
6. G. Consolati, A. Bertin, M. Lanza et al., A new anti-neutrino detection technique based on positronium tagging with plastic scintillators. Nucl. Instrum. Methods A **795**, 364 (2015). https://doi.org/10.1016/j.nima.2015.06.021
7. M. Battaglieri, F. Lippi, G. Rossetti et al., An anti-neutrino detector to monitor nuclear reactor's power and fuel composition. Nucl. Instrum. Methods A **617**, 209 (2010). https://doi.org/10.1016/j.nima.2009.09.031
8. N.S. Bowden, J. Smith, A. Johnson et al., Experimental results from an antineutrino detector for cooperative monitoring of nuclear reactors. Nucl. Instrum. Methods A **572**, 985 (2007).
9. T. Classen, J. Müller, K. Schmidt et al., Development of an advanced antineutrino detector for reactor monitoring. Nucl. Instrum. Methods A **771**, 139 (2015). https://doi.org/10.1016/j.nima.2014.10.022
10. M. Kandemir, A. Cakir, A reactor antineutrino detector based on hexagonal scintillator bars. Nucl. Instrum. Methods A **953**, 163251 (2020).
11. M.H. Liao, K.X. Huang, Y.M. Zhang et al., A ROOT-based detector geometry and event visualization system for JUNO-TAO. Nucl. Sci. Tech. **36**, 39 (2025). https://doi.org/10.1007/s41365-024-01604-0
12. Y.D. Zeng, J. Wang, R. Zhao et al., Decomposition of fissile isotope antineutrino spectra using convolutional neural network. Nucl. Sci. Tech. **34**, 79 (2023). https://doi.org/10.1007/s41365-023-01229-9
13. F.P. An, X. Zhang, Y. Liu et al., Observation of Electron-Antineutrino Disappearance at Daya Bay. Phys. Rev. Lett. **108**, 171803 (2012). https://doi.org/10.1103/PhysRevLett.108.171803
14. J. Cao, Detection methods at reactor neutrino experiments. Nucl. Instrum. Methods A **732**, 9 (2013). https://doi.org/10.1016/j.nima.2013.05.076
15. F. Reines, C.L. Cowan Jr., The neutrino. Nature **178**, 446 (1956). https://doi.org/10.1038/178446a0
16. F.P. An, X. Zhang, Y. Liu et al., The detector system of the Daya Bay reactor neutrino experiment. Nucl. Instrum. Methods A **811**, 133 (2016). https://doi.org/10.1016/j.nima.2015.11.144
17. M. Abbes, J.L. Lagniel, P.G. Rancoita et al., The Bugey 3 neutrino detector. Nucl. Instrum. Methods A **374**, 164 (1996). https://doi.org/10.1016/0168-9002(96)00220-3
18. A. Cabrera, The Double Chooz detector. Nucl. Instrum. Methods A **617**, 473 (2010). https://doi.org/10.1016/j.nima.2009.10.115
19. X.G. Cao, Y.L. Chang, K. Chen et al., NνDEx-100 conceptual design report. Nucl. Sci. Tech. **35**, 3 (2024). https://doi.org/10.1007/s41365-023-01360-7
20. G.M. Chen, X. Zhang, Z.Y. Yu et al., Discrimination of *pp* solar neutrinos and ^{14}C double pile-up events in a large-scale LS detector. Nucl. Sci. Tech. **34**, 137 (2023). https://doi.org/10.1007/s41365-023-01295-z

21. D. Hellfeld, J. Müller, A. Schmidt et al., Reconstructing the direction of reactor antineutrinos via electron scattering in Gd-doped water Cherenkov detectors. Nucl. Instrum. Methods A **841**, 130 (2017). https://doi.org/10.1016/j.nima.2016.10.027
22. D.W. Si, Y. Zhou, S. Xiao et al., Measurement of the high energy γ -rays from heavy ion reactions using Cerenkov detector. Nucl. Sci. Tech. **35**, 24 (2024). https://doi.org/10.1007/s41365-024-01368-7
23. Z. Li, Y. Wang, H. Zhang et al., Atmospheric neutrinos and proton decay in Super-Kamiokande and Hyper-Kamiokande. Nucl. Particle Phys. Proc. **287**, 147 (2017). https://doi.org/10.1016/j.nuclphysbps.2017.03.064
24. S. Kasuga, T. Hayakawa, S. Joukou et al., A study on the eμ identification capability of a water Čerenkov detector and the atmospheric neutrino problem. Phys. Lett. B **379**, 241–247 (1996). https://doi.org/10.1016/0370-2693(96)00138-4
25. K. Clark, M. Smith, A. Johnson et al., IceCube/DeepCore and IceCube/PINGU: Prospects for Few-GeV Scale ν Physics in the Ice. Nucl. Phys. B, Proc. Suppl. **233**, 123 (2012). https://doi.org/10.1016/j.nuclphysbps.2012.12.081
26. Z.P. Ye, Y. Liu, X. Zhang et al., A multi-cubic-kilometre neutrino telescope in the western Pacific Ocean. Nat. Astron. **7**, 1497–1505 (2023). https://doi.org/10.1038/s41550-023-02087-6
27. M. Ageron, J.J. Martin, P.D. Charpak et al., ANTARES: The first undersea neutrino telescope. Nucl. Instrum. Methods A **656**, 11 (2011). https://doi.org/10.1016/j.nima.2011.01.002
28. Y. Sestayo, Search strategies for discovering extraterrestrial neutrinos with IceCube. Nucl. Instrum. Methods A **626–627**, S196 (2011). https://doi.org/10.1016/j.nima.2010.06.264
29. A. Avrorin, A. Shabelski, N.S. Karpov et al., The Baikal neutrino experiment. Nucl. Instrum. Methods A **626–627**, S13 (2011).
30. U.F. Katz, The KM3NeT project. Nucl. Instrum. Methods A **626–627**, S57 (2011). https://doi.org/10.1016/j.nima.2010.06.207
31. J. Brunner, The ANTARES neutrino telescope—Status and first results. Nucl. Instrum. Methods A **626–627**, S19 (2011). https://doi.org/10.1016/j.nima.2010.06.232
32. R. Lahmann, Neutrino detection, position calibration and marine science with acoustic arrays in the deep sea. Nucl. Instrum. Methods A **725**, 32 (2013). https://doi.org/10.1016/j.nima.2012.12.107
33. G. Riccobene, Long-term measurements of acoustic background noise in very deep sea. Nucl. Instrum. Methods A **604**, S149-S157 (2009). https://doi.org/10.1016/j.nima.2009.03.195
34. The Water Cherenkov Simulator (WCSim). Repository. https://github.com/WCSim
35. R.S.J. Purser, Fibonacci grids: A novel approach to global modelling. Quart. J. Roy. Meteorol. Soc. **132**, 619 (2006). https://doi.org/10.1256/qj.05.116
36. K. Abe, T. Takahashi, M. Nakayama et al., Calibration of the Super-Kamiokande detector. Nucl. Instrum. Methods A **737**, 253 (2014).
37. Z.P. Ye, F. Hu, W. Tian et al., A multi-cubic-kilometre neutrino telescope in the western Pacific Ocean. Nat. Astron. **7**, 1497–1505 (2023).
38. K. Lande, P. Wildenhain, The homestake chlorine solar neutrino experiment-past, present and future. Nucl. Phys. B **92**, 563–570 (2003). https://doi.org/10.1016/S0920-5632(03)01303-3
39. D. Hellfeld, A. Bernstein, S. Dazeley et al., Reconstructing the direction of reactor antineutrinos via electron scattering in Gd-doped water Cherenkov detectors. Nucl. Instrum. Methods A **847**, 104–111 (2017). https://doi.org/10.1016/j.nima.2016.10.027
40. A.E. Ball, A. Braem, L. Camilleri et al., C2GT: intercepting CERN neutrinos to Gran Sasso in the Gulf of Taranto to measure θ_{13}. Eur. Phys. J. C **50**, 267–281 (2007). https://doi.org/10.1140/epjc/s10052-006-0193-3
41. J. Caravaca, F.B. Descamps, B.J. Land et al., Experiment to demonstrate separation of Cherenkov and scintillation signals. Phys. Rev. C **95**, 055801 (2017). https://doi.org/10.1103/PhysRevC.95.055801
42. A. Blondel, M. Campanelli, M. Fechner, Energy reconstruction in quasi-elastic events: unfolding physics and detector effects. J. Phys. G Nucl. Part. Phys. **29**, 370–383 (2003). https://doi.org/10.1088/0954-3899/29/8/370
43. S.Y. Zhang, Y.B. Huang, M. He et al., Sub-GeV events energy reconstruction with 3-inch PMTs in JUNO. Nucl. Sci. Tech. **36**, 84 (2025). https://doi.org/10.1007/s41365-025-01678-4
44. M. Shiozawa, A study on the development of high-efficiency detectors. Nucl. Instrum. Methods A **433**, 240 (1999). https://doi.org/10.1016/S0168-9002(99)00038-0
45. E.R. Davies, *Machine Vision: Theory, Algorithms, Practicalities* (Academic Press, San Diego, 1997)
46. D. Cozza, D. Di Bari, A. Di Mauro et al., Recognition of Cherenkov patterns in high multiplicity environments. Nucl. Instrum. Methods A **485**, 700–709 (2002). https://doi.org/10.1016/S0168-9002(01)01625-4
47. T. Alexopoulos, G. Iakovidis, S. Leontsinis et al., Identification of circles from datapoints using the Legendre transform. Nucl. Instrum. Methods A **745**, 16–23 (2014). https://doi.org/10.1016/j.nima.2014.01.046
48. R.E. Twogood, F.G. Sommer, Digital image processing. IEEE Trans. Nucl. Sci. **29**, 1275–1283 (1982). https://doi.org/10.1109/TNS.1982.4336327
49. C. Giunti, C.W. Kim, *Fundamentals of Neutrino Physics and Astrophysics* (University Press, Oxford, 2007)
50. V.M. Fyodorov, Muon registration under water in the ocean with a Cherenkov detector. Nucl. Instrum. Methods A **249**, 514–517 (1986). https://doi.org/10.1016/0168-9002(86)90517-6
51. K. Mitsui, Y. Kawashima, I. Nakamura, The observation of Cherenkov light from the decay of ^{40}K. Nucl. Instrum. Methods A **240**, 465–467 (1985). https://doi.org/10.1016/0168-9002(85)90932-5
52. F. Ameli, M. Bonori, F. Massa, Optical background measurement in a potential site for the NEMO KM undersea neutrino telescope. Eur. Phys. J. C **24**, 117–124 (2002). https://doi.org/10.1007/s10052-002-1015-x
53. D.C. Argento, J.O. Stone, L.K. Fifield et al., Chlorine-36 in seawater. Nucl. Instrum. Methods B **268**, 1949–1953 (2010). https://doi.org/10.1016/j.nimb.2009.10.139
54. M. Bé, V. Chisté, C. Dulieu et al., Table of Radionuclides (Vol. 5 $A = 22$ to 244), 22, Sevres: Bureau International des Poids et Mesures, 2010
55. X.J. Xu, Y. Li, Z. Wang et al., Solar neutrino physics. Prog. Part. Nucl. Phys. **131**, 104043 (2023). https://doi.org/10.1016/j.ppnp.2023.104043